



# Modeling Low-Platinum-Loading Effects in Fuel-Cell Catalyst Layers

Wonseok Yoon\* and Adam Z. Weber\*\*<sup>z</sup>

Environmental Energy Technologies Division, Lawrence Berkeley National Laboratory, Berkeley,  
California 94720, USA

The cathode catalyst layer within a proton-exchange-membrane fuel cell is the most complex and critical, yet least understood, layer within the cell. The exact method and equations for modeling this layer are still being revised and will be discussed in this paper, including a 0.8 reaction order, existence of Pt oxide, possible non-isopotential agglomerates, and the impact of a film resistance towards oxygen transport. While the former assumptions are relatively straightforward to understand and implement, the latter film resistance is shown to cause increased mass-transport limitations with low Pt-loading catalyst layers. Model results demonstrate that the increased oxygen flux and/or diffusion pathway through the film can substantially decrease performance. Also, some scale-up concepts from the agglomerate scale to the more macroscopic porous-electrode scale are discussed and the resulting optimization scenarios investigated.

© 2011 The Electrochemical Society. [DOI: 10.1149/1.3597644] All rights reserved.

Manuscript submitted March 24, 2011; revised manuscript received May 12, 2011. Published June 15, 2011.

The catalyst layer (CL) is a very complex chemical and geometric environment for electrochemical reactions in proton-exchange-membrane fuel cells (PEMFCs). It is composed of supported catalyst particles, ionomer, and gas pores. The reaction occurs at sites where various reacting species such as protons, electrons, and gases meet. Modeling the structure has been approached by various means,<sup>1</sup> and a rigorous mathematical model of the CL is required to capture transport within the different phases, electrochemical reaction, and heat and water generation. Among previous models, one of the most accepted models is an agglomerate particle composed of the ionomer, gas voids, liquid water, and catalyst that is covered by a thin film of ionomer.<sup>2–28</sup> This idea is supported by various experimental observations such as scanning-electron- and transmission-electron-microscopy studies. In this model, oxygen is dissolved in the ionomer film surrounding the agglomerate, and the dissolved oxygen diffuses to the agglomerate where simultaneous transport and reaction occur. Typically, the agglomerate model is embedded (i.e., distributed uniformly across the CL) into a porous-electrode model to describe the CL fully.<sup>1</sup>

Optimization of the CL for enhancing PEMFC performance is of great interest for researchers and industry. Parametric studies of CLs were accomplished by Yin using an agglomerate model,<sup>14</sup> with the model predicting the general polarization-curve trend as a function of parameters such as gas void fraction<sup>7,16</sup> and ionomer<sup>4,5,10,29</sup> and catalyst loadings<sup>5,7,10,30</sup> within the CL. Similarly, several optimization studies<sup>7,16,22</sup> using an agglomerate model were conducted to obtain optimum design parameters such as catalyst loading, CL thickness, and Pt/C ratio for best performance at a given potential. However, all of the studies were based on several assumptions and issues that are not validated or possibly incorrect including a lack of ionomer films and a first-order oxygen dependence for the oxygen-reduction reaction (ORR).

For an agglomerate particle radius of  $0.1 \mu\text{m}$ , the ratio of heat generation to conduction is about 0.01 using typical PEMFC properties, demonstrating that the particle will remain isothermal, even with the relatively thin, thermally resistive ionomer skin.<sup>31</sup> Similarly, electron diffusion is not limiting and the particles can be assumed to be electronically isopotential. However, due to a structure in which there may be water or gas filling the agglomerates or due to possibly low conductivity of the ionomer within the CL, it is unclear as to whether the particles can be assumed to be ionically isopotential. In addition, the ORR within a fuel-cell CL has been shown to not be first order,<sup>32</sup> which is often assumed. Finally, the thin ionomer film around the agglomerate particles can limit the oxygen flux through the particles, and this should be evaluated.

One of the barriers against the commercialization of PEMFCs is the material cost, with the dominant one being that of Pt. Therefore, numerous research has focused on developing effective and economical ways to reduce the Pt loading without impacting overall performance (i.e., increase the mass activity). For traditional CLs, there are two main routes to lower the Pt loading. The first is to decrease the Pt/C ratio and the second is to make the CL thinner. Both cases though seem to have a limit in that unexplained resistances occur at very low loadings ( $<0.1 \text{ mg/cm}^2$ ),<sup>30</sup> that do not occur at higher loadings.<sup>33</sup> This effect has not been fully explained, and simulation is required to justify and explain the prevalent theories. It is thought that the resistance is due to changes in the kinetics due to the increased turnover rate required per Pt particle, resistance through the ionomer layer and/or agglomerate, or even contamination and poisoning.

In this paper, the kinetics and transport phenomena using an agglomerate model are systematically explored, including appropriate expressions for the overall rate expression. Both agglomerate (1-D) and CL (1 + 1D) simulations are accomplished for the cathode CL. Below, we first discuss the modeling approach and examine both relevant kinetic and transport assumptions and effects. Next, some CL layer optimization with regards to agglomerate particles is explored as well as the impact of mass-transport limitations at low Pt loadings.

## Theory

**Governing equations.**—Here, we consider a single spherical particle of radius  $R_a$  with ionomer film having a thickness of  $\delta_{\text{film}}$  at an arbitrary local point within the cathode CL as shown in Fig. 1(a). Since no assumptions are made regarding proton and oxygen mass-transport, the two transport equations must be solved simultaneously

$$\nabla \cdot (\kappa_m \nabla \Phi_2) + j_e = 0 \quad [1]$$

and

$$\nabla \cdot (D_e \nabla C_{O_2}) + j_{O_2} = 0 \quad [2]$$

respectively, where  $D_e$  is the effective diffusion coefficient of dissolved oxygen inside the particle,  $C_{O_2}$  is the oxygen concentration in the particle,  $j_{O_2}$  is oxygen molar consumption rate,  $\kappa_m$  is the ionomer phase conductivity,  $\Phi_2$  is the ionomer-phase potential, and  $j_e$  is the oxygen-reduction-reaction rate. It should be noted that accurate estimations or measurements of the diffusion coefficient and ionomer conductivity inside the particle remain elusive. In this study, reasonable values, some from literature and some from estimation, are used; and, where appropriate, they are varied to assess their impact. Essentially, it is believed that the agglomerate core is

\* Electrochemical Society Student Member.

\*\* Electrochemical Society Active Member.

<sup>z</sup> E-mail: azweber@lbl.gov

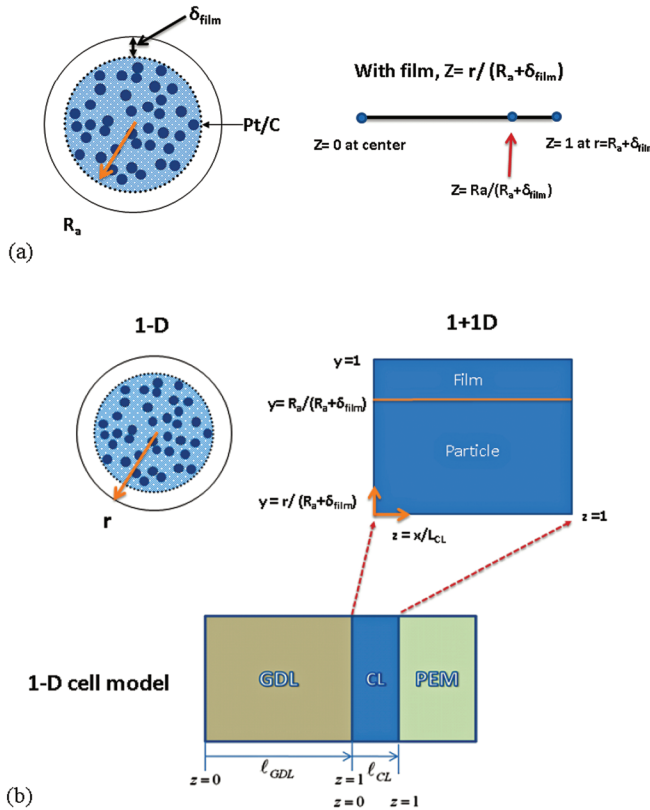


**Figure 1.** (Color online) (a) Illustration of an agglomerate particle and 1-D computational domain of the particle used for this study and (b) illustration of dimensionless 1-D cathode model (PEM is not modeled).

filled with liquid water or a very tortuous pathway, and so has a diffusion coefficient on the order of oxygen in water.

Before proceeding, one should note that another equation of the form of Eq. 2 could be written for the product water. In the analysis in this paper, this was found to not be limiting on the agglomerate scale; thus water transport is only considered at the layer and sandwich scale. Furthermore, the simulations given are for conditions in which liquid water is not dominant (e.g., non-f fully-humidified feeds), so as not to complicate the results and obscure the conclusions with not fully understood two-phase flow phenomena. However, the possible existence of liquid-water films is discussed and shown to be a straightforward extension of the present analysis without rendering any of the findings invalid.

To implement Eqs. 1 and 2, they are written in spherical coordinates (radial direction) and nondimensionalized. For example, the final equation form of the diffusion equation can be described as

$$\frac{1}{z^2(R_a + \delta_{film})} \frac{d}{dz} \left( z^2 D_e \frac{1}{(R_a + \delta_{film})} \frac{dC_{O_2}}{dz} \right) + j_{O_2} = 0 \quad [3]$$

where  $z = r/(R_a + \delta_{film})$  in the particle and

$$\frac{d}{dz} \left( z^2 D_{film} \frac{1}{(R_a + \delta_{film})} \frac{dC_{O_2}}{dz} \right) = 0 \quad [4]$$

in the ionomer film.

The source terms for the two governing equations above are given as

$$j_{O_2} = -k_{c,n} C_{O_2}^n \quad [5]$$

and

$$j_e = -4Fk_{c,n} C_{O_2}^n \quad [6]$$

where

$$k_{c,n} = (1 - \theta_{PtOH}) \frac{i_{ref}}{4FC_{ref,O_2}^n} \exp\left(-\frac{\alpha_c F}{RT} \eta_c\right) \quad [7]$$

$$i_{ref} = a_{pt} \cdot i_0 = \frac{L_{ca} A_{ca}}{\ell_{CL}} \cdot i_{0,s}^* \exp\left[\frac{-E_c^{rev}}{RT} \left(1 - \frac{T}{T^*}\right)\right] \quad [8]$$

where  $\theta_{PtOH}$  is the Pt-oxide coverage,  $k_{c,n}$  is the reaction rate constant,  $i_{ref}$  is the ORR exchange current density,  $a_{pt}$  is the specific platinum surface area per unit catalyst layer volume,  $\ell_{CL}$  is the thickness of the catalyst layer,  $E_c^{rev}$  is the activation energy of the ORR at the reversible cell potential,  $T^*$  is the reference temperature.

The catalyst loading,  $L_{ca}$ , and electrochemical surface area,  $A_{ca}$ , are the critical parameters in determining PEMFC performance. To account for those effects, the exchange current density ( $A/cm^2 P_i$ ) is based on active Pt area and the volumetric exchange current density is obtained by multiplying the catalyst specific current density by  $L_{ca} A_{ca}/\ell_{CL}$ . In this study, typical surface areas for Pt catalysts are used.

For the boundary conditions, the oxygen concentration and overpotential are specified at the surface of the ionomer film and symmetry is used at the agglomerate center.

To determine the relative importance of transport phenomena and kinetics in an agglomerate, an effectiveness-factor approach is used.<sup>34,35</sup> The effectiveness factor,  $E_r$ , can be described as a ratio of the actual reaction rate to a rate if the entire interior surface is exposed to the conditions outside of the particle

$$E_r = \frac{4\pi R_a^2 \left( -D_e \frac{dC_{O_2}}{dr} \Big|_{r=R_a} \right)}{\frac{4}{3}\pi R_a^3 (-k_{s,n} C_{O_2,s}^n)} \quad [9]$$

The overall reaction rate is described by multiplication of the effectiveness factor by a rate constant and the surface-oxygen concentration. Most CL models using a particle model employ the effectiveness-factor approach for calculating the ORR.<sup>11,13,16,35-37</sup> For a first-order reaction with no other transport limitations, an analytic expression for the effectiveness factor is obtained<sup>12,14,35</sup>

$$E_r = \frac{3}{\Phi^2} (\Phi \coth \Phi - 1) \quad [10]$$

where  $\Phi$  is the Thiele modulus

$$\Phi = R_a \sqrt{\frac{k_{c,s,n} C_{O_2,s}^{n-1}}{D_e}} \quad [11]$$

*Kinetics.*—In this study, the overpotential is used as the variable of interest in the agglomerate particle.<sup>15,38</sup> Since the solid-phase potential is assumed uniform within the particle and using a reference oxygen electrode, the cathode overpotential can be reduced to

$$\eta_c = \Phi_1 - \Phi_2 - U = \Phi_1 - \Phi_2 \quad [12]$$

and a potential gradient in the ohm's law for ionic current can be replaced by the gradient of local overpotential

$$\nabla \eta_c = \nabla \Phi_1 - \nabla \Phi_2 = -\nabla \Phi_2 \quad [13]$$

where  $\Phi_1$  and  $\Phi_2$  are the solid- and ionomer-phase potentials, respectively, and  $U$  is the theoretical local equilibrium potential of a cathode with respect to the reference O<sub>2</sub> electrode.

The local cathode potential (local cell voltage) can be approximately calculated by<sup>38</sup>

$$\Phi_1 = E + \eta_c \quad [14]$$

$$E = E_O^0 + \frac{RT}{4F} \ln(P_{x_{O_2,in}}) \quad [15]$$

The four electron ORR involves several intermediate oxides' adsorption and desorption process which can make understanding the process more difficult. Platinum oxides form at the potential range of the ORR (0.6–1.0 V) by water or gas-phase oxygen. These oxides can prohibit the ORR by blocking active Pt sites. Typically, a constant Tafel slope for the ORR kinetics around 60 to 70 mV/decade is assumed over the cathode potential range relevant to PEMFC operation. However, it has been suggested by experiments that this approach has to be modified to account for the potential-dependent oxide coverage as shown in Eq. 7.<sup>39–41</sup> Several forms of oxide can exist; OH coverage is considered in this study. It is further assumed that the existence of the oxide eliminates the reaction on that site and does not fundamentally change the reaction mechanism; therefore such factors as the oxygen reaction order should remain the same in both cases. The kinetic expression for the platinum oxidation and equilibrium coverage (i.e., at steady state) are given by

$$\frac{d\theta_{PtOH}}{dt} = k_{PtOH} \left( (1 - \theta_{PtOH}) \exp\left(\frac{\alpha'_a F}{RT} \eta_{PtOH}\right) - \theta_{PtOH} \exp\left(\frac{-\alpha'_c F}{RT} \eta_{PtOH}\right) \right) \quad [16]$$

$$\theta_{PtOH} = \frac{\exp\left[\frac{\alpha'_a F}{RT} \eta_{PtOH}\right]}{\exp\left[\frac{\alpha'_a F}{RT} \eta_{PtOH}\right] + \exp\left[\frac{-\alpha'_c F}{RT} \eta_{PtOH}\right]} \quad [17]$$

$$\eta_{PtOH} = \Phi_s - \Phi_m - U_{PtOH} \quad [18]$$

where  $k_{PtOH}$ ,  $\eta_{PtOH}$ , and  $U_{PtOH}$  are the Pt-oxidation rate constant, overpotential, and equilibrium potential, respectively.

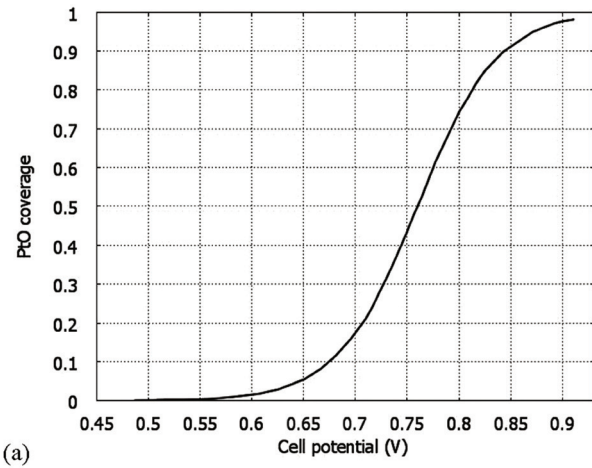
Figure 2 examines the impact of the oxide-coverage effect. A transfer coefficient,  $\alpha_c$ , is set to 1 for the case when the Pt oxide is not taken into account and to 0.5 for the case when the Pt-oxide coverage is included in the ORR kinetic expression. This correction accounts for the observed Tafel slope of around 120 mV/decade when the oxide term is included.<sup>40</sup> As can be seen in Fig. 2(a), the Pt-oxide coverage decreases as the cell potential decreases. This surface coverage affects the agglomerate current density at higher cell potentials (low overpotentials) due to the blockage of active sites by chemisorbed surface oxygen. The Pt-oxide term causes the Tafel slope to be potential dependent.<sup>41</sup> Figure 2(b) displays the impact of the Pt-oxide on a polarization curve using the half-cell model described below. The exchange current densities for the two cases are adjusted in a way that the current densities have the same value at a cell potential of 0.9 V, where most of the kinetic parameters have been measured.<sup>32</sup> At high cell potentials, the difference between the two cases is not obvious in this plot, but the cathode model for the case when the oxide coverage is considered produces higher current density at the same cell potential below 0.9 V and lower current density above 0.9 V as compared to the case of not considering Pt oxide. At middle potentials, the PtOH curve shows a more gentle behavior, which agrees better with typical experimental polarization curves. At low potentials, the curves become diffusion limited and approach each other; Pt oxide does not have an effect.

Another key kinetic parameter is the oxygen reaction order. This value is widely assumed to be a value of 1, based on studies during the last couple of decades,<sup>42–47</sup> although other values have been obtained with Pt alloys.<sup>48</sup> However, these studies were done in liquid electrolytes and using rotating-disk-electrode methods. Relatively recently, Gasteiger and coworkers<sup>49,50</sup> and Xu et al.,<sup>51</sup> conducted detailed experiments and analyses showing that under fuel-cell conditions and CL structures, the ORR oxygen reaction order is around 0.8 (referenced to an imaginary hydrogen reference electrode with its

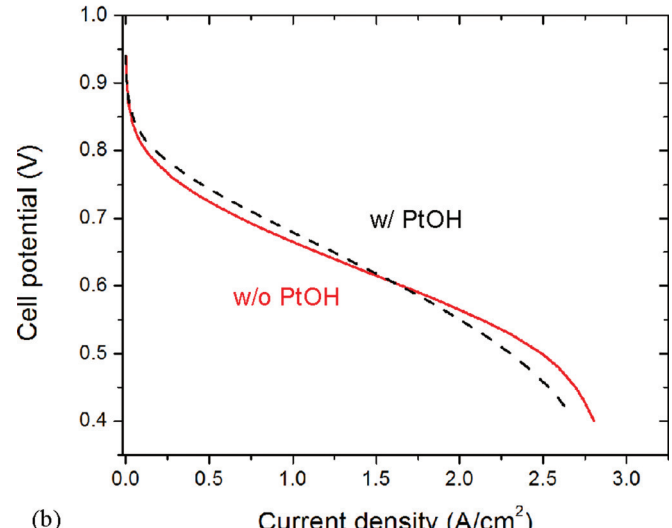
own extraneous phases, i.e., the standard reversible potential) and not 1. This non-unity reaction order makes the diffusion equation become nonlinear and numerical solution is required to obtain the effectiveness factor. In general, as the reaction order increases, the effectiveness factor decreases for the same Thiele modulus.

Figure 3(a) explores the impact of the reaction order by showing simulated polarization curves with the two different reaction orders (note that the simulated performance is relatively good since certain effects such as contact resistances and ohmic losses in the bulk membrane are not considered). It is clear that the performance curve with the reaction order of 0.8 is higher than the performance curve of the first-order reaction, since the oxygen partial pressure is always below its reference value. Non-unity reaction orders make the Thiele modulus dependent on the reactant concentration and thus the effectiveness factor varies with the reactant concentration. Figure 3(b) shows the variation of the effectiveness factor with respect to oxygen concentration at different overpotentials. At low overpotential,  $\eta_c = -0.38$  V ( $\sim 0.8$  V cell potential), the difference in the effectiveness factor is too small to differentiate one from the other, but at high overpotential,  $\eta_c = -0.68$  V ( $\sim 0.5$  V cell potential), the effectiveness factor for the reaction order of 0.8 clearly deviates from the value for the first-order reaction.

Figure 3 clearly demonstrates that the reaction order impacts PEMFC behavior. However, such a treatment requires numerical solvers since the Thiele modulus now depends on reactant



(a)



**Figure 2.** (Color online) (a) Platinum oxide coverage in terms of cell potential and (b) performance curve of the cathode model with and without the PtO coverage.

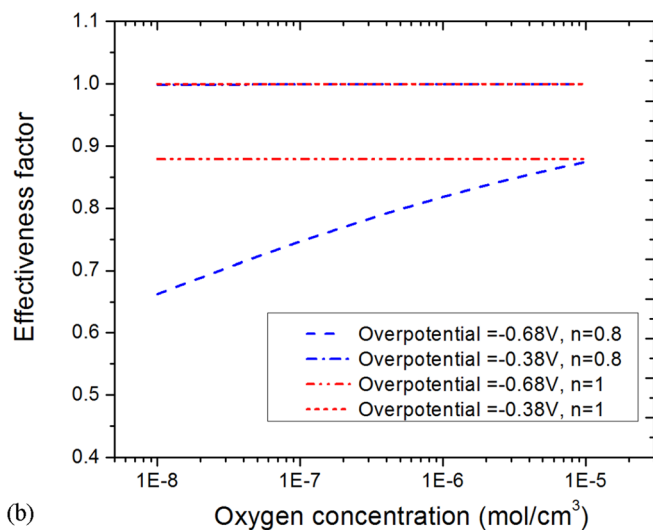
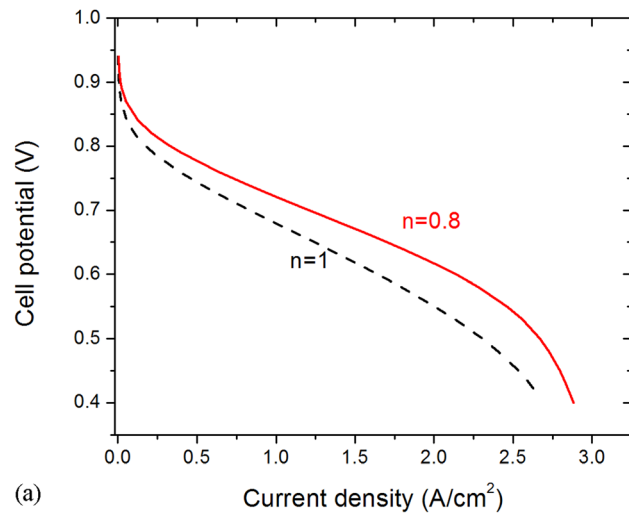


**Figure 3.** (Color online) Simulated (a) polarization curves and (b) effectiveness-factor variation with respect to oxygen concentration when the reaction order is 1 and 0.8.

concentration. One simple approach is to use the Thiele modulus with the reaction order ( $n$ ) set to 0.8 (see Eq. 11) with the effectiveness factor Eq. 10 derived for a first-order reaction. As shown in Fig. 4, such an approach only results in minimal error, which is sufficient for most modeling purposes. It is therefore recommended that if the equipotential assumption is valid, one just uses the modified Thiele modulus in the effectiveness factor expression. For the rest of this manuscript, a reaction order of 0.8 is used.

**Transport.**—As noted above, assumptions of protonic isopotential and isothermal conditions are often made. As discussed, the isothermal assumption is valid, and indeed our simulations confirm this unless the heat conductivity is dramatically low ( $\sim 1 \times 10^{-6} \text{ W}/\text{cmK}$ ), which is 3 orders of magnitude below that of bulk Nafion,<sup>52</sup> and the oxygen diffusion coefficient inside the agglomerates is high ( $\sim 1 \times 10^{-3} \text{ cm}^2/\text{s}$ ), thereby reacting near the core and keeping the heat within the particle. To examine the isopotential assumption, the proton conductivity is varied from  $10^{-7}$  to 0.1 S/cm. Figure 5(a) shows the overpotential at the center of the particle. The overpotential remains at the same level of the surface overpotential when the conductivity varies from 0.1 to around  $10^{-4} \text{ S}/\text{cm}$ , but increases significantly when the conductivity decreases further down to  $10^{-7} \text{ S}/\text{cm}$ . This result indicates that the isopotential

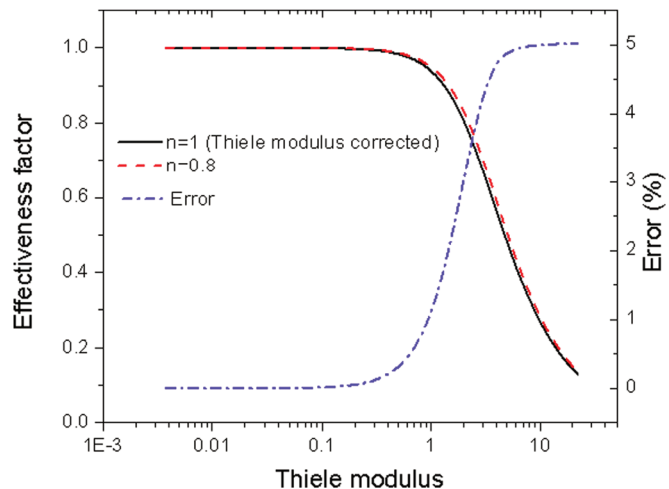


**Figure 4.** (Color online) Comparison of the effectiveness factor from the analytic solution with Thiele modulus corrected for 0.8 reaction order ( $n$ ), and the numerically calculated effectiveness factor for  $n = 0.8$ .

assumption is not valid if the proton conductivity is below  $10^{-4} \text{ S}/\text{cm}$  or so. Under these conditions, the effectiveness factor and current density are significantly impacted, as shown in Fig. 5(b), especially at higher overpotentials (lower cell potentials). While for typical CLs, it is believed that the ionomer conductivity is sufficiently

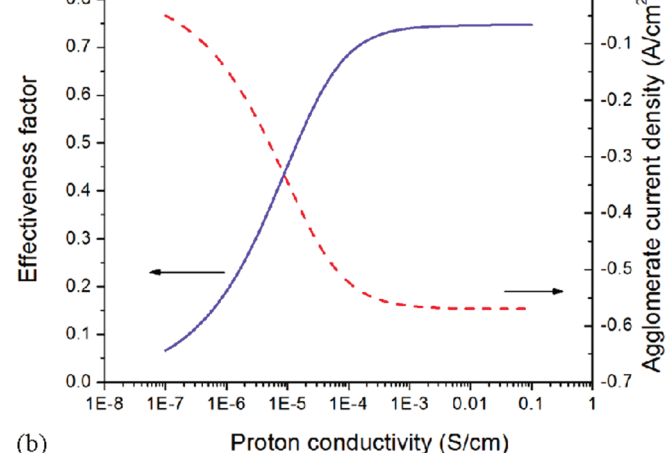
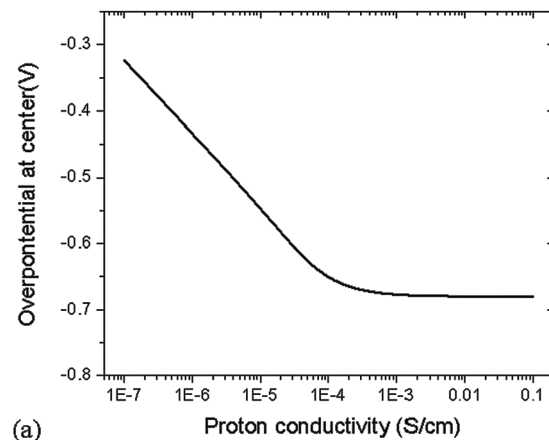


**Figure 5.** (Color online) (a) Overpotential profile at center of the agglomerate particle with respect to proton conductivity and (b) the effectiveness factor and agglomerate current density at the surface of the particle (The surface overpotential is  $-0.68\text{V}$  which corresponds to a cell potential of  $\sim 0.5\text{ V}$ ).

above the critical value,<sup>53–55</sup> it remains to be measured unequivocally. In addition, one can envision cases, such as at very low humidities, where the conductivity is below this threshold value. Furthermore, recent molecular-dynamic studies<sup>56,57</sup> have shown that the inside of the agglomerate may not be filled with ionomer due to its chain-length size, thus suggesting that the conductivity within the agglomerate is very low or close to that of pure water (although there are ionic contaminants). While this issue needs some more experimental investigation, for most cases the assumption of uniform ionic potential is probably valid.

In general, the agglomerates are surrounded by an ionomer film that retards oxygen mass transport.<sup>11,12,14</sup> Since the exact properties and thickness of the film are unknown, a resistance approach (ratio of the film thickness,  $\delta$ , and permeation coefficient,  $\psi$ ) is used to represent the oxygen transport resistance of the film<sup>58</sup>

$$N_{O_2} = -D_{film}\nabla C_{O_2,diss} = -\frac{D_{film}H}{RT}\nabla P_{O_2,ext} = -\psi_{O_2}\nabla P_{O_2,ext} \quad [19]$$

$$R_{O_2,film} = \frac{\delta_{film}}{\psi_{O_2}} \quad [20]$$

where  $R_{O_2,film}$  is the transport resistance of oxygen through ionomer film and  $P_{O_2,ext}$  is the partial pressure of the oxygen outside of the film. In addition, one can imagine a liquid-water film around particles as well. In terms of diffusion, a liquid-water film has a similar effect as an ionomer film, and thus adding a liquid-water film is equivalent to changing the film transport resistance (adjusting for the respective transport properties and thicknesses of the films) in the above treatment.

To evaluate the importance of the film, one can compare the external (including film) and internal (no film limitations) effectiveness factors, where both are defined in a similar manner as actual reaction rate over the rate if outside conditions are present everywhere (see Eq. 9). Figure 6 shows the overall and internal effectiveness factors with respect to film resistance. As can be seen, there is a steep drop of the overall effectiveness factor showing how a film quickly can limit oxygen concentration and performance. For reference, assuming bulk-Nafion properties, a resistance of  $0.01 \text{ m}^2 \text{ s bar/mol}$  is equivalent to a film thickness of 11 nm; however, the thin ionomer film could be more glassy and thus have lower gas transport than the bulk membrane.<sup>59,60</sup>

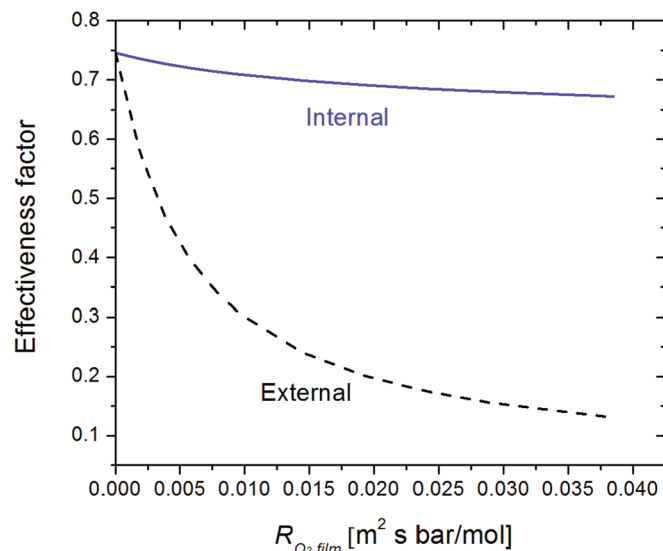


**Figure 6.** (Color online) Overall and internal effectiveness factors as a function of ionomer-film oxygen resistance (see equation 20) at a surface overpotential of  $-0.68 \text{ V}$ .

*Half-cell model.*—The agglomerate model developed above is coupled with a macroscopic porous CL model to examine the effects of model parameters for the particle models on PEMFC performance. This means that the coupled physical phenomena in different length scales need to be solved together. In this study, this coupling is realized by using a 1 + 1D, non-dimensional approach for particle models as shown in Fig. 1(b). The z-direction denotes the dimensionless length across the CL and the y direction indicates the radial direction of each particle located in a position z. For the particle model in the 1 + 1D space, all the fluxes such as oxygen diffusion flux and current flow are defined in the y direction only, and the fluxes through the z-direction are enforced to be negligible.

This 1 + 1D particle model can provide reaction source terms that are required in cell-level models, such as oxygen consumption rate per volume of the CL and reaction current per volume of the CL.<sup>38</sup> The general equations can be expressed by

$$J_{O_2} = -\frac{(1-\varphi_c)}{4\pi(R_a + \delta_{film})^3/3} \cdot (4\pi R_a^2) \frac{D_e}{(R_a + \delta_{film})} \frac{\partial C_{O_2}}{\partial y} \Big|_{y=\frac{R_a}{R_a + \delta_{film}}} \quad [21]$$

$$= -\frac{(1-\varphi_c)}{4\pi(R_a + \delta_{film})^3/3} \cdot [4\pi(R_a + \delta_{film})^2] \frac{D_{film}}{(R_a + \delta_{film})} \frac{\partial C_{O_2}}{\partial y} \Big|_{y=1} \quad [22]$$

$$J_e = -\frac{(1-\varphi_c)}{4\pi(R_a + \delta_{film})^3/3} \cdot [4\pi(R_a + \delta_{film})^3] \int_0^{\frac{R_a}{R_a + \delta_{film}}} 4Fk_{c,n}C_{O_2}^n y^2 dy \quad [23]$$

where  $\varphi_c$  is gas phase porosity in the CL,  $J_{O_2}$  is the oxygen consumption rate, and  $J_e$  is the reaction current per unit volume in the CL, calculated from the 1 + 1D agglomerate particle models.

Gas-phase transport in the gas-diffusion layer (GDL) and CL is described by multicomponent diffusion, Stefan-Maxwell equation and liquid water is not considered in this model (the gases are assumed to be humidified but remain subsaturated).

$$\frac{1}{\ell} \nabla x_i = \sum_{j \neq i} \frac{x_i N_j - x_j N_i}{c_T D_{ij}^{eff}} \quad [24]$$

$$D_{ij}^{eff} = \varphi^{1.5} D_{ij}^o \quad [25]$$

$$D_{ij}^o(T, P) = D_{ij}^o(T_1, P_1) \times \frac{P_1}{P} \times \left(\frac{T}{T_1}\right)^{1.8} \quad [26]$$

In above equations,  $D_{ij}^{eff}$  is the effective binary interaction parameter between species i and j described by Bruggeman relation,  $\ell$  is the length of GDL or CL, and  $c_T$  is the total concentration of all of the gas species.

For the cathode, oxygen, water vapor, and nitrogen are considered and mass-balance equations for the oxygen and water vapor in the porous region result in the following expressions (assuming that nitrogen flux equals zero since it does not participate in the reactions)

$$\frac{1}{\ell} \nabla \cdot (c_T v_G x_i) = -\frac{1}{\ell} \nabla \cdot N_i + S_i \text{ in the GDL and CL} \quad [27]$$

where  $S$  is the corresponding source term, and

$$v_G = -\frac{k_G}{\mu_G} \frac{1}{\ell} \nabla P_G \quad [28]$$

To keep the analysis simple and since liquid water is not explicitly modeled, viscosity,  $\mu_G$ , and permeability,  $k_G$ , are assumed constant. It should be noted that the permeability is sufficiently large that the impact of convection on the simulation results is minimal for the conditions explored in this paper; Eq. 28 is included for completeness. Source terms for oxygen and water vapor in GDL and CL can be expressed as follows:

**Table I.** Boundary conditions for 1D cathode model.

Variable	Ch/GDL	GDL/CL	CL/Mem
$x_{O_2}$	$x_{O_2}$ given	$N_o _{z=1,GDL} = N_o _{z=0,CL}$	$N_o _{z=1,CL} = 0$
$\omega$	$\omega$ given	$N_\omega _{z=1,GDL} = N_\omega _{z=0,CL}$	$N_\omega _{z=1,CL} = 0$
$P_G$	$P_G$ given	$N _{z=1,GDL} = N _{z=0,CL}$	$N _{z=1,CL} = 0$
$\Phi_s$	$\Phi_s$ given	$\frac{1}{\ell_{GDL}} \sigma_{GDL}^{eff} \nabla \Phi_s \Big _{z=1,GDL}$ $= \frac{1}{\ell_{CL}} \sigma_{CL}^{eff} \nabla \Phi_s \Big _{z=0,CL}$	$\nabla \Phi_s, z = 1, CL = 0$
$\Phi_m$	N/A	$\nabla \Phi_m, z = 0, CL = 0$	$\Phi_m = 0$

$$S_{O_2} = 0, \quad S_{H_2O(v)} = 0 \text{ in GDL} \quad [29]$$

$$S_{O_2} = J_{O_2}, \quad S_{H_2O(v)} = -\frac{1}{2} J_e (1 + 2n_d)/F \text{ in the CL} \quad [30]$$

Electron transport and proton transport are described by Ohm's law

$$\frac{1}{\ell} \nabla \cdot \left( \sigma_s^{eff} \frac{1}{\ell} \nabla \Phi_s \right) - S = 0 \text{ in the GDL and CL} \quad [31]$$

$$\frac{1}{\ell} \nabla \cdot \left( \kappa_m^{eff} \frac{1}{\ell} \nabla \Phi_m \right) + S = 0 \text{ in the CL} \quad [32]$$

$$S = 0 \text{ in the GDL, and } S = J_e \text{ in the CL} \quad [33]$$

Boundary conditions for all of the physics are tabulated in Table I. It should be noted that 1+1D agglomerate particle models require

the oxygen concentration and overpotential profile across the CL as boundary conditions ( $0 < z < 1$ ,  $y = 1$ , in Fig. 1(b)). All other exterior boundary conditions are insulation except for internal boundary between ionomer film and particle, which is continuity.

## Results and Discussions

The agglomerate and half-cell models described above are employed to examine the PEMFC performance and to investigate how the CL structure can impact performance as well as the impact of the film resistance for low Pt-loading electrodes. For all of the analyses below, the full 1+1D model described above with an oxygen transport resistance of  $R_{O_2,film} = 0.01 \text{ m}^2 \text{ s bar/mol}$  is used. The agglomerate particle radius is assumed to be  $0.1 \mu\text{m}$  and the other model parameters used for the simulation are listed in Table II.

*Catalyst-Layer Optimization.*—To understand the reaction-rate distribution, Fig. 7 shows the effectiveness factor and rate profiles at various cell potentials. The reaction rate is uniform at high potentials and becomes much more nonuniform at lower ones. For the set of properties used in these simulations, the dominant loss is the low proton conductivity in the ionomer due to the low RH used. This limitation causes a higher rate near the Mem/CL boundary, although at high current densities oxygen losses begin to become increasingly important, thereby changing the shape of the distribution and making it more parabolic.

It is of interest to examine how the agglomerate-size distribution can impact PEMFC performance. To do this, first, a set of optimization studies is performed for the case when the film thickness or resistance (see Eq. 20) varies proportionally with the particle radius. The ratio of the film thickness and particle radius is fixed to a value

**Table II** Model parameters for baseline simulation of agglomerate particle models and CL models.

Parameter	Value
Temperature	$T$ $80^\circ\text{C}$
Total gas pressure	$P$ $1.1 \text{ bar}$
Particle radius	$R_a$ $0.1 \mu\text{m}$
Oxygen inlet mole fraction	$x_{O_2,in}$ $0.15$
Water vapor inlet mole fraction	$\omega_{in}$ $0.22$
Surface oxygen concentration for the particle model	$C_s$ $1 \times 10^{-7} \text{ mol/cm}^3$
Cathodic transfer coefficient (with Pt oxide)	$\alpha_c$ $0.5$
Cathodic transfer coefficient (w/o Pt oxide)	$\alpha'_c$ $1$
Equilibrium potential	$E_O^o$ $1.2 \text{ V}$
ORR exchange current density (with Pt oxide)	$i_{0,s}^*$ $6.0 \times 10^{-3} \text{ A/cm}^2_{\text{Pt}}$
ORR exchange current density (w/o Pt oxide)	$i_{0,s}^*$ $1.5 \times 10^{-6} \text{ A/cm}^2_{\text{Pt}}$
CL porosity <sup>a</sup>	$\varphi_c$ $0.1, 0.6$
GDL porosity	$\varphi_{GDL}$ $0.4$
CL thickness	$\ell_{CL}$ $15 \mu\text{m}$
GDL thickness	$\ell_{GDL}$ $300 \mu\text{m}$
Pt loading	$L_{ca}$ $0.2 \text{ mg}_{\text{Pt}}/\text{cm}^2$
Electrochemical surface area	$A_{ca}$ $40 \text{ m}^2_{\text{Pt}}/\text{g}_{\text{Pt}}$
Activation energy of the ORR at the reversible cell potential (Ref. 32)	$E_c^{\text{rev}}$ $67 \text{ kJ/mol}$
Reference temperature (Ref. 32)	$T^*$ $353 \text{ K}$
Electro-osmotic coefficient	$n_d$ $1$
Ionomer conductivity in film and particle	$\kappa_m$ $0.01 \text{ S/cm}$
Oxygen permeation coefficient in ionomer film (Refs. 12, 58)	$\psi_{film}$ $1 \times 10^{-11} \text{ mol/s} \cdot \text{cm} \cdot \text{bar}$
Effective oxygen diffusion coefficient in the particle	$D_e$ $8.45 \times 10^{-5} \text{ cm}^2/\text{s}$
Equilibrium potential for Pt oxide formation	$U_{\text{PtO}}$ $0.76 \text{ V}$
Anodic transfer coefficient for Pt oxide formation	$\alpha_a$ $0.4$
Cathodic transfer coefficient for Pt oxide formation	$\alpha'_c$ $0.4$
Oxygen/water vapor diffusion coefficient <sup>38</sup> ( $T_1 = 308 \text{ K}, P_1 = 1 \text{ atm}$ )	$D_{O_2,H_2O}$ $0.282 \text{ cm}^2/\text{s}$
Oxygen/Nitrogen diffusion coefficient <sup>38</sup> ( $T_1 = 316 \text{ K}, P_1 = 1 \text{ atm}$ )	$D_{O_2,N_2}$ $0.230 \text{ cm}^2/\text{s}$
Nitrogen/water vapor diffusion coefficient <sup>38</sup> ( $T_1 = 298 \text{ K}, P_1 = 1 \text{ atm}$ )	$D_{N_2,H_2O}$ $0.293 \text{ cm}^2/\text{s}$
Effective permeability of gas phase (GDL)	$k_G$ $1 \times 10^{-9} \text{ cm}^2$
Effective permeability of gas phase (CL)	$k_G$ $1 \times 10^{-11} \text{ cm}^2$
Viscosity of gas phase	$\mu_G$ $2.1 \times 10^{-5} \text{ Pa s}$

<sup>a</sup>For the normal or slow diffusion case, 0.1 is used; for the fast diffusion, 0.6 is used.

of 0.1, which corresponds to the ratio of 10 nm film thickness and 0.1  $\mu\text{m}$  particle radius. The first case being examined is that when the particle radius varies linearly from 10 to 190 nm from GDL side to membrane side and the second case is the opposite gradient; the average particle radius is 0.1  $\mu\text{m}$  for all cases. Figure 8(a) shows the polarization curves of the two cases and the baseline (uniform) case. Interestingly, the particle distribution from large to small size (GDL to membrane) generates small performance increases in the high-current-density region than the other cases. The comparison of the average effectiveness factor (averaged over the CL thickness) for the three cases reveals that the usage of catalyst particles for the third case can be maximized at the given distribution pattern. Since the oxygen concentration is highest at the GDL/CL boundary and lowest at the CL/membrane boundary, large particles at the GDL/CL and small particles at the CL/membrane can maximize utilization of the catalyst particles. However, when the film thickness (resistance) is fixed at a constant value (which may be more realistic of the actual microstructure), both gradient cases show lower performance compared to the uniform baseline, which can be seen in Fig. 8b. This is because the film has a larger and counter effect for the small particles and thus limits the performance increase even though there is a gain from the large particles. Overall, these simulations show that optimization of particle size within the CL does not seem to provide a great benefit and may not be easy to obtain, espe-

cially when one considers that under operation the virgin distribution undoubtedly evolves.

**Low Pt-loading electrodes.**—As mentioned, very low Pt-loading electrodes are recently being fabricated and explored to reduce PEMFC cost. However, experimental studies show that both reducing the Pt/C ratio or the CL thickness results in additional mass-transfer limitations.<sup>30,61</sup> It is thought that this may be due to the increased oxygen flux to the Pt surface as shown in Fig. 9.<sup>30,62</sup> Here, we explore both effects as shown in Fig. 9.

Reducing the CL thickness can be easily implemented by changing the thickness parameter in the dimensionless governing

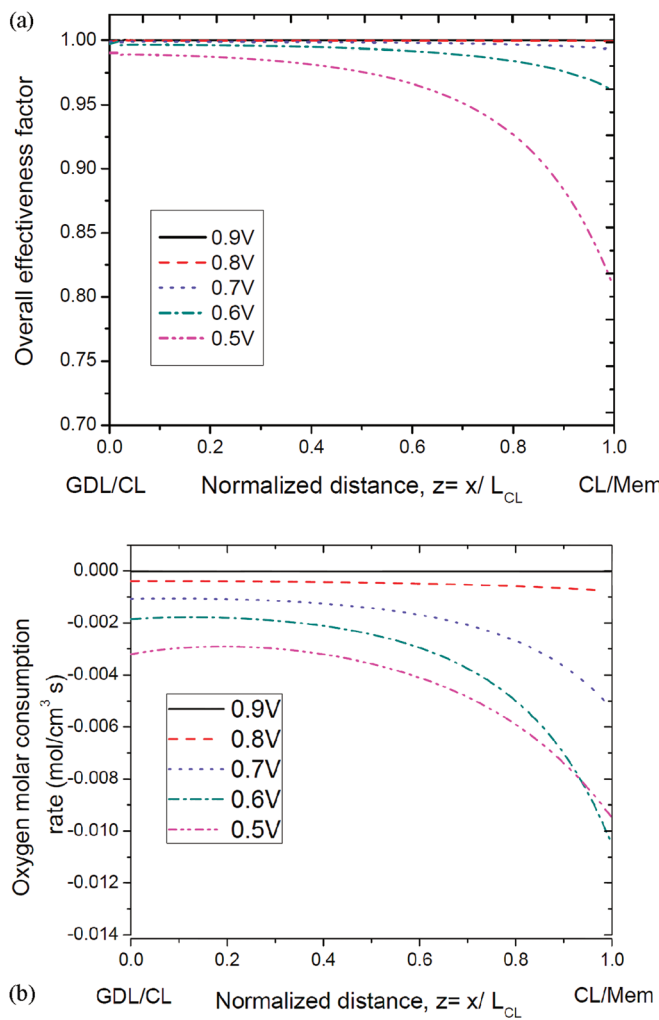


**Figure 7.** (Color online) (a) Overall effectiveness-factor profile and (b) oxygen molar-consumption rate at different cell potentials across the catalyst layer.

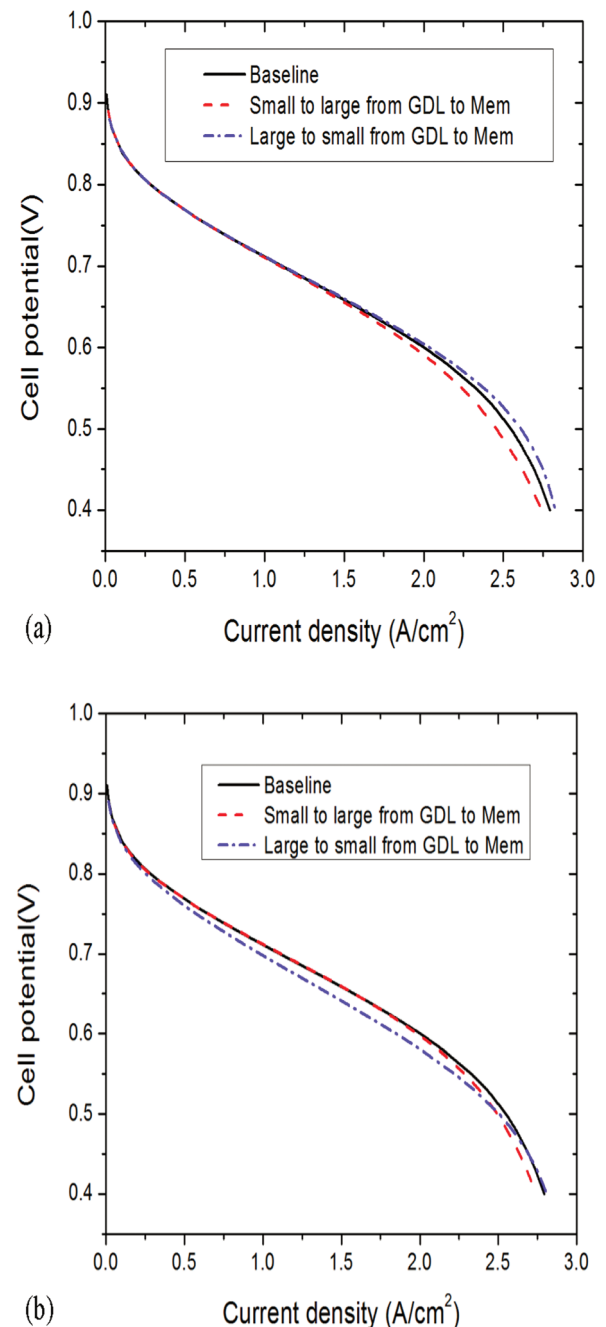


**Figure 8.** (Color online) (a) Comparison of polarization curves for the cases of three different particle distributions when the film thickness varies proportionally and (b) when the film oxygen resistance is constant,  $R_{O_2,\text{film}} = 0.01 \text{ m}^2 \text{ s bar/mol}$ .

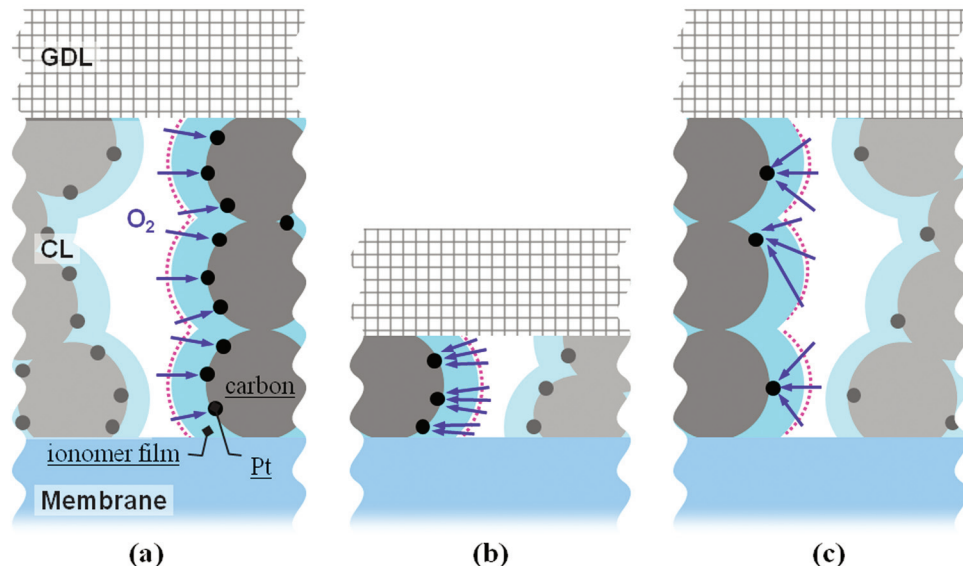


**Figure 9.** (Color online) Schematic image of oxygen transport through the ionomer film for (a) normal CL structure and two low Pt-loading cases, (b) thinner CL, and (c) low Pt/C ratio. Figure adopted from Ref. 30.

equations; however, there is another parameter that needs to be adjusted as well: the Pt loading. Typically, the Pt loading is calculated by measuring the total weight of Pt ( $mg_{Pt}$ ) deposited in the CL followed by dividing it by the geometric electrode area ( $cm^2_{geo}$ ). Therefore, Pt loading decreases as the CL thickness decreases due to the reduction of the total amount of Pt deposited in the CL. However, to see the impact of decreasing Pt loading by changing CL thickness, one is required to keep the volumetric Pt loading ( $L_{ca}/l_{CL}$ ,  $mg_{Pt}/cm^3$ ) constant for all CL thicknesses. Since the same composition of catalyst ink is used for fabrication of CLs with different thicknesses, this should be a correct approach to account for the CL-thickness effect. The electrochemical surface area (ECSA) also needs to be measured for different Pt loadings and taken into account in the modeling, and, for this study, a constant roughness-factor ( $cm^2_{Pt}/cm^2_{geo}$ ) is used as derived from Table II.

Polarization curves for three different CL thickness, 15, 10, and 5  $\mu m$  are plotted in Fig. 10. Comparison of the polarization curves with and without ionomer film reveals that at low current density, performance of the PEMFC with the thin CL is lower than that with the thick CL due to the decreased Pt loading. However, at high current density, the performance with the thinner CL increases for both cases with and without ionomer film, although not linearly with CL thickness. Specifically, when the CL thickness is 5  $\mu m$ , the rate of performance increase is limited due to the film in agreement with the analysis of Kudo et al.,<sup>60</sup> but still shows a slightly higher performance than the 10  $\mu m$  thick case. The reason for the higher performance at the high-current-density region can be explained by better transport of protons and oxygen in the layer, thereby making the reaction distribution more uniform and at a higher current density (see Fig. 7).

To examine the upper bound for oxygen transport in the CL, a higher porosity is used in the model, thus minimizing the diffusional resistance. These conditions are more in-line with those of Nonoyama et al.,<sup>30</sup> who mention that they observed no significant oxygen mass-transport limitations in their CLs. Using the higher porosity, the simulations are rerun at two different cell potentials (0.8 and 0.5 V), and the normalized value of the current density is plotted as a function of CL thickness and four different film transport resistances in Fig. 11. For the cell potential of 0.5 V (Fig. 11(b)), the comparison of the film and no-film curves show that the PEMFC performance with the film decreases with decreasing CL thickness, indicating that the oxygen transport loss in these CL structures

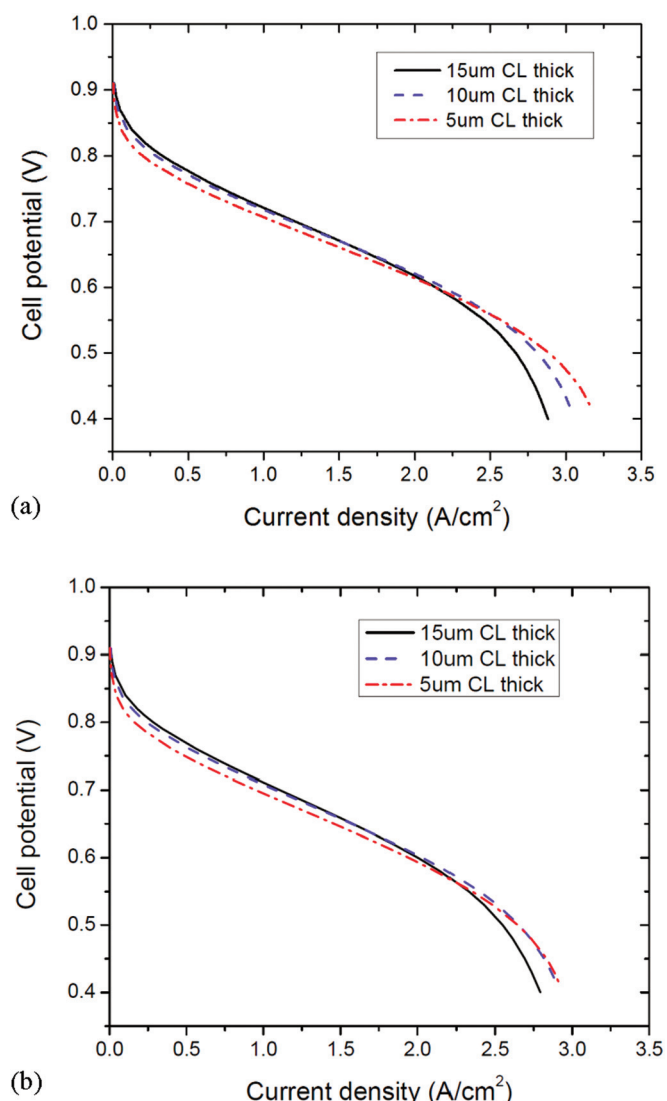


**Figure 10.** (Color online) Polarization curves without (a) and with (b) ionomer film for three different CL thicknesses,  $R_{O_2, film} = 0.01 \text{ m}^2 \text{ s bar/mol}$ .

outweighs the loss of electrochemical reaction volume. In addition, the film causes a significant change in the limiting current. This implies that for thin CLs with low Pt loadings, the ionomer film covering the agglomerate can become limiting and a significant barrier to mass transport, in accordance with Fig. 9 and the data of Nonoyama et al.<sup>30</sup> and, to a lesser extent, the changes seen by Shinozaki et al.<sup>62</sup> However, at low current density (0.8 V cell potential), the relative PEMFC performance decreases greatly with decreasing the CL thickness as plotted in Fig. 11(c) (although the absolute value of the change is not that large as seen in Fig. 10). This result implies that the performance is not limited by transport in the CL in agreement with the uniform distribution for this case in Fig. 7b; the normalized current density with the high porosity almost overlaps the plot with the low one. Both cases show that the film adds mass-transport resistance which increases steeply (and nonlinearly) as the CL thickness decreases. The curves also demonstrate that at higher oxygen resistances, the bend in the curve occurs with thicker CLs (higher Pt loadings).

The other method of lowering the Pt content is by diluting it by decreasing the Pt/C ratio for the same CL thickness and carbon particle size. To further investigate this phenomenon, simulations were conducted with lower loading values in the same modeling framework as that above (not shown). However, there was no discernable change in performance beyond the kinetic effect, which is counter to what has been seen experimentally. The lack of any change demonstrates that the kinetics (or turnover frequency) of oxygen on the Pt surface is not limiting, and that the existing model cannot accurately capture any increased mass-transfer limitations. Thus, a more realistic model is required to fully analyze this case. Unlike the lower loadings due to the change in CL thickness, decreasing the Pt/C ratio impacts the local agglomerate picture in that there are now less Pt atoms exposed for reaction per unit volume. Coupled with the increased flux to the reaction site since there are less Pt atoms, the impact is that diffusion becomes less and less 1-D and more multidimensional including both the radial and other directions since oxygen must diffuse along the other directions to reach the sporadic active sites; this additional diffusion path needs to be accounted for.

To explore this diffusional path in more detail, 2-D simulations of a particle surface are conducted. In this study, a quarter of an agglomerate particle is modeled with a 10 nm thick ionomer film and a 10 nm reaction volume (although this is not critical to the analysis); the modeling domain is shown in Fig. 12a. A total of twelve equivalent reaction zones were created and distributed uniformly along the circumference of the particle. To mimic the different loading cases, the number of activated (reaction can occur) and deactivated (no reaction) reaction zones is controlled while keeping the distance between adjacent reaction zones as uniform as possible. The case numbers and corresponding zones are given in Table III. This approach mimics the fact that at lower Pt/C ratios, the Pt sites on the agglomerate surface become more isolated from each other. While it is true that the secondary agglomerate structure or size may be impacted by different Pt/C ratios, since this is dominated by the carbon-carbon interactions and these particles remain the same size, it is expected that the agglomerate size does not change significantly. Furthermore, since relatively high current density operation is being examined, it is appropriate to just examine the reaction at the surface of the agglomerate (see Fig. 7). For boundary conditions, an oxygen flux equivalent to an agglomerate current density of 0.025 A/cm<sup>2</sup> is applied to the exterior surface of the film for all cases as well as constant oxygen concentration and temperature. As an example, the resulting oxygen flux and concentration for cases #1 and #12 are shown in Fig. 12b and 12c, respectively. From the simulation results, the average concentration of oxygen around the reaction-zone boundaries is calculated through numerical integration.

Figure 13 shows the normalized (to case #1) oxygen concentration for all the different cases. The normalized concentrations are around unity for most of the cases until the last few, where it

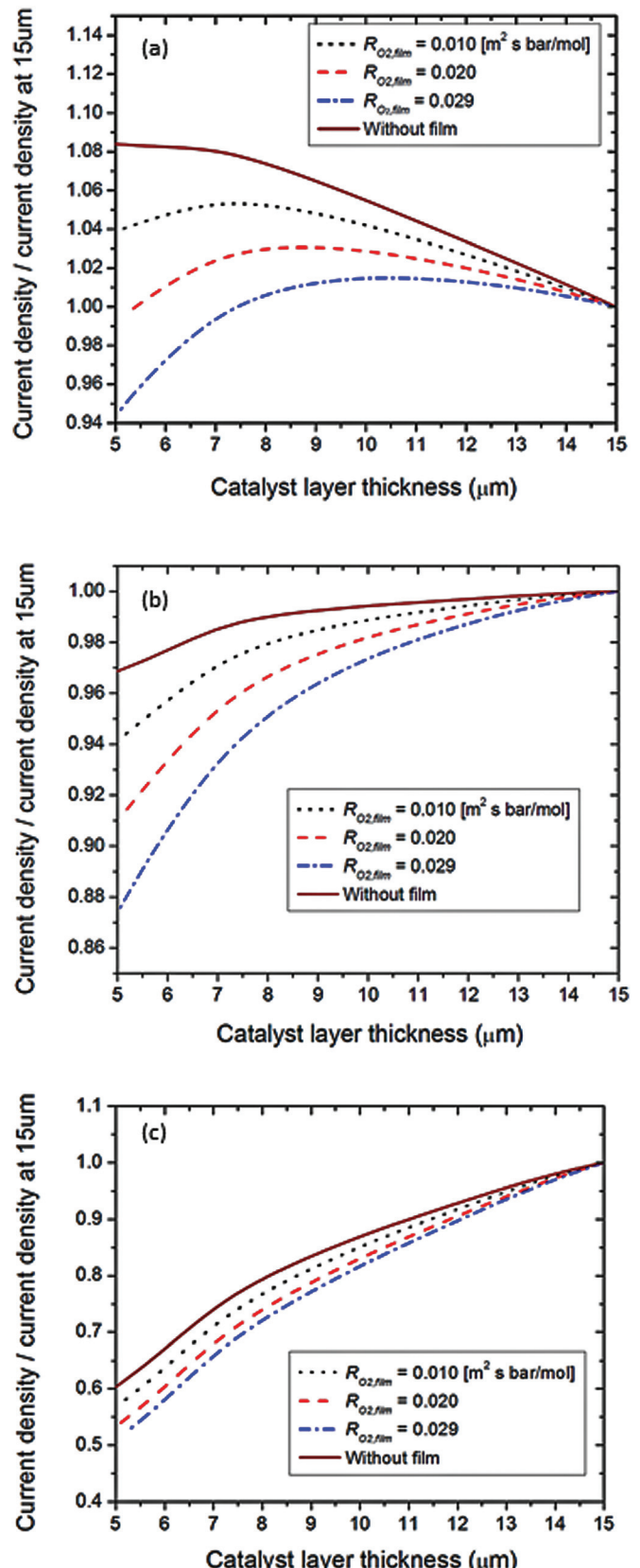


**Figure 11.** (Color online) Current density at 0.5 V with different film thicknesses with respect to the CL thickness (a) baseline diffusion coefficients (low CL porosity), (b) fast diffusion coefficients (high CL porosity) in the CLs, and (c) current density at 0.8 V with different film thicknesses with respect to the CL thickness using baseline diffusion coefficients.

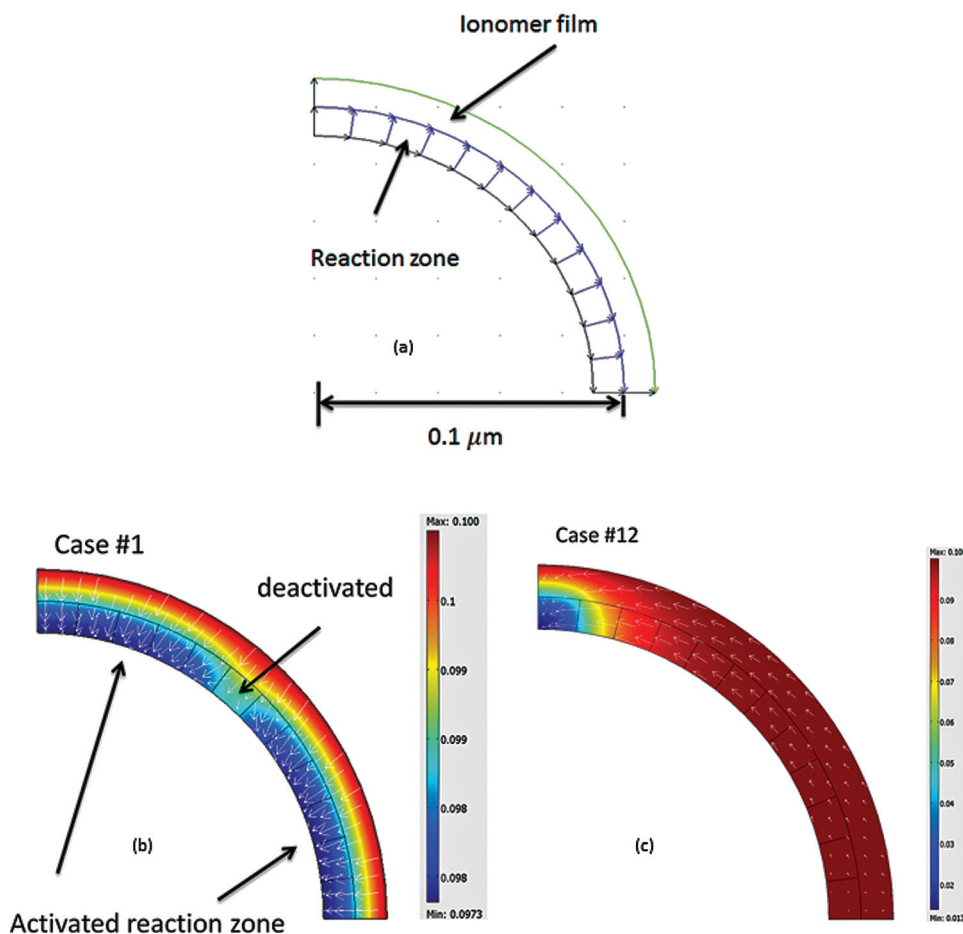


**Figure 12.** (Color online) (a) Computational domain of two dimensional simplified agglomerate particle model,  $R_{O_2, \text{film}} = 0.01 \text{ m}^2 \text{ s bar/mol}$  (b) a simulation result showing oxygen concentration ( $\text{mol}/\text{m}^3$ ) and flux for case #1, and (c) at case #12. (Current density of  $0.025 \text{ A}/\text{cm}^2$  at the surface is set).

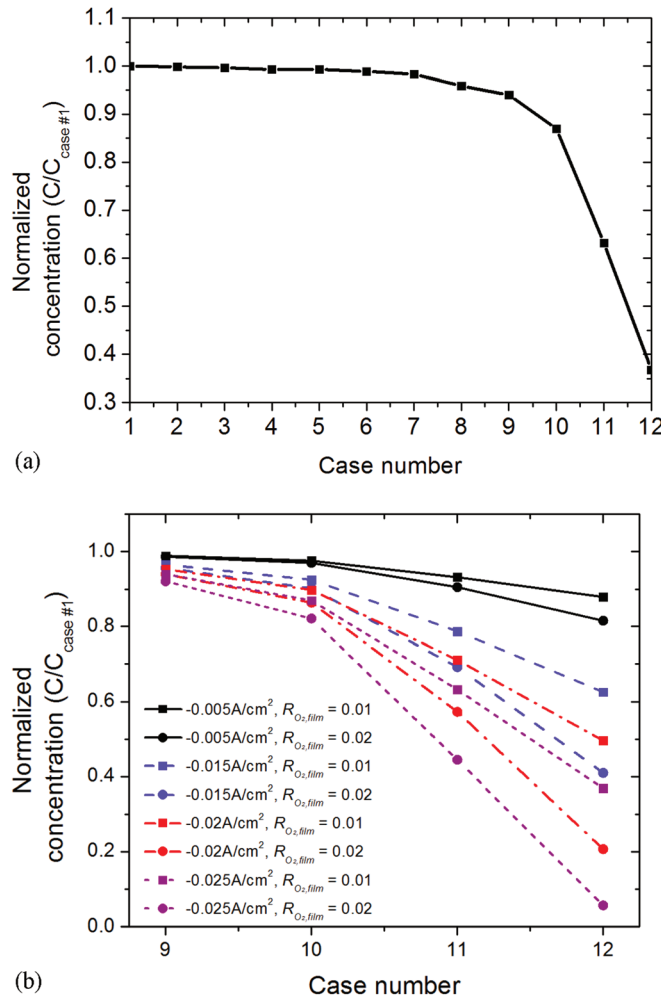
decreases dramatically. A more resistive or thicker film causes a steeper drop as expected. Thus, there seems to be a significant mass-transport limitation at lower loadings. This impact can be seen as an increase in the oxygen diffusion pathway length, and can be used as an effective film thickness in the 1-D calculation, similar to the effective diffusion-media thickness in the treatment of rib/channel 2-D effects.<sup>63</sup> Since Fickian diffusion is assumed through the film, the change in the oxygen concentration is directly related to the same increase in film thickness. Thus, from

Fig. 13, for case #12, the effective thickness is slightly more than half when the active zones or loading is 1/12. Assuming a typical Pt loading of  $0.4 \text{ mg}/\text{cm}^2$  for case #1, this means that the effective thickness is about double around  $0.03 \text{ mg}/\text{cm}^2$ . Overall, the ionomer film causes significant and unexpected mass-transport limitations at very low Pt loadings no matter the cause. However, decreasing the loading by changing the Pt/C ratio rather than the CL thickness seems to enhance the effect due to the more significant impact of oxygen diffusion path length. It should be noted that one would not expect these resistances to exist for agglomerates and CLs that do not contain ionomer films (e.g., extended-surface Pt structures).

A final point is that one may wonder as to the applicability of the above findings since the models ignore liquid-water build-up in the CL, especially at high current density. However, the referenced data and model is geared towards lower humidity operation where one does not have substantial liquid water. Furthermore, the effect of liquid water on transport with respect to the CL structure requires the relationship between capillary pressure and liquid-water saturation for the different structures, something that is not available currently in literature. In addition, while we discuss an ionomer film above, one can also view it as a liquid-water film or a combination of the two. Either type of film would be resistive to oxygen transport with its resistance given by its thickness and permeation coefficient. Thus, the analysis above holds for any type of film resistance. As a final point, if a liquid-water film does exist, one may expect that for the lower loaded catalyst layers its thickness may increase due to the increased reaction rate per platinum particle, which would exacerbate the above discussed mass-transport limitations.

**Table III.** Case number and distribution of activated and deactivated reaction zones for each case ( $O$  = active reaction zone,  $\times$  = deactivated reaction zone).

Case number	Segments from top to bottom											
	O	O	O	O	O	O	O	O	O	O	O	O
1	O	O	O	O	O	O	O	O	O	O	O	O
2	O	O	$\times$	O	O	O	O	O	$\times$	O	O	O
3	O	O	$\times$	O	O	O	$\times$	O	O	$\times$	O	O
4	O	O	$\times$	O	O	$\times$	O	O	$\times$	O	O	$\times$
5	O	$\times$	O	O	$\times$	O	$\times$	O	$\times$	O	$\times$	O
6	$\times$	O	$\times$	O	O	$\times$	O	$\times$	O	$\times$	O	$\times$
7	$\times$	O	$\times$	$\times$	O	$\times$	O	$\times$	O	$\times$	O	$\times$
8	$\times$	$\times$	O	$\times$	$\times$	O	$\times$	$\times$	O	$\times$	$\times$	O
9	$\times$	$\times$	O	$\times$	$\times$	$\times$	O	$\times$	$\times$	O	$\times$	$\times$
10	$\times$	$\times$	O	$\times$	$\times$	$\times$	$\times$	$\times$	O	$\times$	$\times$	$\times$
11	$\times$	$\times$	$\times$	$\times$	$\times$	O	$\times$	$\times$	$\times$	$\times$	$\times$	$\times$
12	O	$\times$										



**Figure 13.** (Color online) (a) Normalized oxygen concentration around the reaction zones,  $R_{O_2,film} = 0.01 \text{ m}^2 \text{ s bar/mol}$  and (b) concentration drop at case #9, 10, 11, and 12 with respect to agglomerate current density and two different film resistances.

## Conclusions

In this paper, a proton-exchange-membrane-fuel-cell cathode catalyst layer is modeled with a focus on explaining mass-transport limitations with low Pt-loaded catalyst layers. The modeling includes the observed effects of Pt oxide, ionomer film, and a 0.8 reaction order with respect to oxygen. In addition, the impact of assuming protonic isopotential conditions was explored with the determination that this assumption is probably valid under most conditions. Simulations of cathode catalyst layers demonstrated that there is not a great benefit to optimizing the agglomerate particle-size distribution. The cathode-catalyst-layer model and a 1 + 1D particle-surface model clearly showed that the ionomer film that covers the agglomerate results in a mass-transport limitation that increases drastically at low Pt loadings. The cause of this was shown to be due to the higher oxygen fluxes through the ionomer film and longer diffusion pathways. While changing Pt loading by decreasing the catalyst-layer thickness or the Pt/C ratio both demonstrate these effects, they are more pronounced in the Pt/C ratio case.

## Acknowledgments

The authors would like to thank Nobuaki Nonoyama and Rohit Makharia for their helpful discussions. Funding for this project was provided by the Assistant Secretary for Energy Efficiency and Renewable Energy, Office of Hydrogen, Fuel Cell, and Infra-

structure Technologies, of the U. S. Department of Energy under contract number DE-AC02-05CH11231 and CRADA agreement LB08003874 between LBNL and Toyota Motor Company.

## List of Symbols

$a_{pt}$	specific platinum surface area per unit catalyst layer volume, $\text{cm}^2_{Pt}/\text{cm}^3_{geo}$
$A_{ca}$	electrochemical surface area, $\text{cm}^2_{Pt}/\text{mg}_{Pt}$
$b$	Tafel slope, V
$C_{O_2}$	oxygen concentration in an agglomerate particle, mol/cm <sup>3</sup>
$c_T$	total concentration of gas phase, mol/cm <sup>3</sup>
$D_e$	effective diffusion coefficient of dissolved oxygen inside the particle, cm <sup>2</sup> /s
$D_{film}$	effective diffusion coefficient of oxygen in ionomer film, cm <sup>2</sup> /s
$D_{ij}^{eff}$	effective binary diffusion coefficient in GDL and CL, cm <sup>2</sup> /s
$E$	equilibrium potential of fuel cell reaction with respect to hydrogen reference electrode, V
$E_c^{rev}$	activation energy of the ORR at the reversible cell potential, kJ/mol
$E_r$	effectiveness factor
$F$	Faraday's constant, 96487 C/equiv
$H$	Henry's constant
$i_{0,s}^*$	catalyst specific exchange current density, A/cm <sup>2</sup> <sub>Pt</sub>
$j_e$	oxygen reduction reaction current in an agglomerate particle, A/cm <sup>3</sup>
$J_e$	reaction current per unit volume of the CL, A/cm <sup>3</sup>
$j_{O_2}$	molar rate of reaction in an agglomerate particle, mol/cm <sup>3</sup> s
$J_{O_2}$	oxygen consumption rate in CL, mol/cm <sup>3</sup> s
$k_{c,n}$	rate constant of oxygen reduction reaction, nth order reaction, varies
$k_G$	effective permeability of the gas phase, cm <sup>2</sup>
$k_{PtOH}$	rate constant for Pt oxidation, 1/s
$l_k$	length of GDL or CL, μm
$N_i$	superficial flux density of species i, mol/cm <sup>2</sup>
$n_d$	osmotic drag coefficient
$L_{ca}$	Pt loading, mg <sub>Pt</sub> /cm <sup>2</sup>
$P$	Total gas phase pressure, pa
$r$	radial coordinate
$R_a$	Particle radius, μm
$R$	universal gas constant, 8.3143 J/mol K
$S$	source term in mass balance equations
$T$	absolute temperature, K
$T^*$	reference temperature, K
$U$	equilibrium potential, V
$v_G$	mass averaged velocity,
$x_{O_2,in}$	inlet Oxygen mole fraction
$x$	mole fraction of oxygen
$y$	nondimensional length in radial direction for 2-D agglomerate model
$z$	nondimensional length in radial direction for 1-D agglomerate model and nondimensional length for 1-D cathode model
Greek	
$\alpha_a$	anodic transfer coefficient
$\alpha_c$	cathodic transfer coefficient
$\theta_{PtOH}$	Platinum oxide coverage
$\delta_{film}$	thickness of ionomer film, nm
$\varepsilon_i$	porosity phase i
$\sigma_s$	conductivity of the electronically conducting phase, S/cm
$\kappa_m$	conductivity of the ionically conducting phase, S/cm
$\Phi_2$	ionomer phase potential, V
$\Phi_1$	solid phase potential, V
$\mu_G$	viscosity of the gas phase, pa s
$\eta_c$	cathode overpotential, V
$\eta_{PtOH}$	overpotential for platinum oxidation, V
$\omega$	water vapor mole fraction
$\psi$	gas permeation coefficient through ionomer film, mol/s m bar
$\Phi$	Thiele modulus
Subscripts	
1	solid, electronically conducting phase
2	membrane, ionically conducting phase
a	anodic
c	cathodic
G	gas phase

s solid phase, agglomerate particle surface  
 m ionomer phase  
 o standard value  
 e effective property  
 diss dissolved  
 ext external

## Superscripts

eff effective property  
 ref value taken at a reference condition

## References

1. A. Z. Weber and J. Newman, *Chem. Rev.*, **104**, 4679 (2004).
2. J. Liu and M. Eikerling, *Electrochim. Acta*, **53**, 4435 (2008).
3. Q. Wang, D. Song, T. Navessin, S. Holdcroft, and Z. Liu, *Electrochim. Acta*, **50**, 727 (2004).
4. Q. Wang, M. Eikerling, D. Song, Z. Liu, T. Navessin, Z. Xie, and S. Holdcroft, *J. Electrochim. Soc.*, **151**, A950 (2004).
5. M. Srinivasarao, D. Bhattacharyya, R. Rengaswamy, and S. Narasimhan, *Chem. Eng. Res Des*, In press. [DOI: 10.1016/j.cherd.2010.04.020]
6. M. Srinivasarao, D. Bhattacharyya, R. Rengaswamy, and S. Narasimhan, *Int. J. Hydrogen Energy*, **35**, 6356 (2010).
7. D. T. Song, Q. P. Wang, Z. S. Liu, M. Eikerling, Z. Xie, T. Navessin, and S. Holdcroft, *Electrochim. Acta*, **50**, 3347 (2005).
8. R. Rosenthal and B. Farhanieh, *Int. J. Hydrogen Energy*, **32**, 4424 (2007).
9. S. Kamarajgadda and S. Mazumder, *J. Power Sources*, **183**, 629 (2008).
10. N. Khajeh-Hosseini-Dalasm, M. J. Kermani, D. Ghadiri Moghaddam, and J. M. Stockie, *Int. J. Hydrogen Energy*, **35**, 2417 (2010).
11. F. Jaouen, G. Lindbergh, and G. Sundholm, *J. Electrochim. Soc.*, **149**, A437 (2002).
12. W. Sun, B. A. Peppley, and K. Karan, *Electrochim. Acta*, **50**, 3359 (2005).
13. K. Broka and P. Ekdunge, *J. Appl. Electrochem.*, **27**, 281 (1997).
14. K. M. Yin, *J. Electrochim. Soc.*, **152**, A583 (2005).
15. R. M. Rao and R. Rengaswamy, *J. Power Sources*, **158**, 110 (2006).
16. M. Secanell, K. Karan, A. Suleman, and N. Djilali, *Electrochim Acta*, **52**, 6318 (2007).
17. D. Gerteisen, A. Hakenjos, and J. O. Schumacher, *J. Power Sources*, **173**, 346 (2007).
18. P. Berg, A. Novruzi, and K. Promislow, *Chem. Eng. Sci.*, **61**, 4316 (2006).
19. S.-M. Chang and H.-S. Chu, *J. Power Sources*, **172**, 790 (2007).
20. M. Chisaka and H. Daiguji, *Electrochim. Commun.*, **8**, 1304 (2006).
21. D. Harvey, J. G. Pharoah, and K. Karan, *J. Power Sources*, **179**, 209 (2008).
22. P. Jain, L. T. Biegler, and M. S. Jhon, *Electrochim. Solid-State Lett.*, **11**, B193 (2008).
23. C.-Y. Jung, C.-H. Park, Y.-M. Lee, W.-J. Kim, and S.-C. Yi, *Int. J. Hydrogen Energy*, **35**, 8433 (2010).
24. S. Obut and E. Alper, *J. Power Sources*, **196**, 1920 (2011).
25. K. M. Yin, *J. Appl. Electrochem.*, **37**, 971 (2007).
26. M. Eikerling, *J. Electrochim. Soc.*, **153**, E58 (2006).
27. Z. Xia, Q. Wang, M. Eikerling and Z. Liu, *Can. J. Chem.*, **86**, 657 (2008).
28. Q. Wang, M. Eikerling, D. Song, and Z. Liu, *J. Electroanal. Chem.*, **573**, 61 (2004).
29. E. Antolini, L. Giorgi, A. Pozio, and E. Passalacqua, *J. Power Sources*, **77**, 136 (1999).
30. N. Nonoyama, S. Okazaki, A. Z. Weber, Y. Ikogi, and T. Yoshida, *J. Electrochim. Soc.*, **158**, B416 (2011).
31. A. A. Kulikovsky, *J. Electroanal. Chem.*, **652**, 66 (2011).
32. K. C. Neyerlin, W. Gu, J. Jorne, and H. A. Gasteiger, *J. Electrochim. Soc.*, **153**, A1955 (2006).
33. H. A. Gasteiger, J. E. Panels, and S. G. Yan, *J. Power Sources*, **127**, 162 (2004).
34. H. S. Fogler, *Elements of Chemical Reaction Engineering*, Prentice Hall Inc. (1992).
35. F. Gloaguen and R. Durand, *J. Appl. Electrochem.*, **27**, 1029 (1997).
36. F. Jaouen and G. Lindbergh, *J. Electrochim. Soc.*, **150**, A1699 (2003).
37. P. Jain, L. T. Biegler, and M. S. Jhon, *J. Electrochim. Soc.*, **157**, B1222 (2010).
38. Q. Guo and R. E. White, *J. Electrochim. Soc.*, **151**, E133 (2004).
39. Y. Liu, M. Mathias, and J. Zhang, *Electrochim. Solid-State Lett.*, **12**, B1 (2010).
40. J. X. Wang, J. Zhang, and R. R. Adzic, *J. Phys. Chem. A*, **111**, 12702 (2007).
41. S. Gottesfeld, *ECS Trans.*, **6**(25), 51 (2008).
42. A. Parthasarathy, S. Srinivasan, A. J. Appleby, and C. R. Martin, *J. Electrochim. Soc.*, **139**, 2856 (1992).
43. A. Parthasarathy, S. Srinivasan, A. J. Appleby, and C. R. Martin, *J. Electronanal. Chem.*, **339**, 101 (1992).
44. D. B. Sepa and M. V. Vojnovic, *Electrochim. Acta*, **26**, 781 (1981).
45. D. B. Sepa, M. V. Vojnovic, and L. M. Vrancar, *Electrochim. Acta*, **32**, 129 (1987).
46. A. J. Appleby, *J. Electrochim. Soc.*, **117**, 328 (1970).
47. U. A. Paulus, T. J. Schmidt, H. A. Gasteiger, and R. J. Behm, *J. Electroanal. Chem.*, **495**, 134 (2001).
48. S. Mukerjee and S. Srinivasan, *J. Electroanal. Chem.*, **357**, 201 (1993).
49. K. C. Neyerlin, W. Gu, J. Jorne, A. Clark, and H. A. Gasteiger, *J. Electrochim. Soc.*, **154**, B279 (2007).
50. K. C. Neyerlin, H. A. Gasteiger, C. K. Mittelstaedt, J. Jorne, and W. B. Gu, *J. Electrochim. Soc.*, **152**, A1073 (2005).
51. H. Xu, Y. Song, H. R. Kunz, and J. M. Fenton, *J. Electrochim. Soc.*, **152**, A1828 (2005).
52. M. Khandelwal and M. M. Mench, *J. Power Sources*, **161**, 1106 (2006).
53. Y. Sone, P. Ekdunge, and D. Simonsson, *J. Electrochim. Soc.*, **143**, 1254 (1996).
54. J. Fang, X. Guo, S. Harada, W. Tatsuya, K. Tanaka, H. Kita, and K.-i. Okamoto, *Macromolecules*, **35**, 9022 (2002).
55. R. Makaria, M. F. Mathias, and D. R. Baker, *J. Electrochim. Soc.*, **152**, A970 (2005).
56. T. Mashio, K. Malek, M. Eikerling, A. Ohma, H. Kanesaka, and K. Shinohara, *J. Phys. Chem. C*, **114**, 13739 (2010).
57. M. E. Hannach, in *Proceedings of the 61st Annual Meeting of the International Society of Electrochemistry*, Nice, France (2010).
58. A. Z. Weber and J. Newman, *J. Electrochim. Soc.*, **151**, A311 (2004).
59. Y. Huang and D. R. Paul, *Polymer*, **45**, 8377 (2004).
60. K. Kudo, T. Suzuki, and Y. Morimoto, *ECS Trans.*, **33**(1), 1217 (2010).
61. K. Shinozaki, H. Yamada, and Y. Morimoto, *ECS Trans.*, **33**(1), 1217 (2010).
62. K. Shinozaki, H. Yamada, and Y. Morimoto, *J. Electrochim. Soc.*, **158**, B467 (2011).
63. A. Z. Weber, *Electrochim. Acta*, **54**, 311 (2008).